Characteristic Analysis of Parallel and Anti-Parallel Coupled Line Structures and Their Integrated Design in Filtering Power Dividers

Daotong Li, *Senior Member, IEEE*, Luqi Zhang, Jiaxin Wang, *Graduate Student Member, IEEE*, Ying Liu, and Qiang Chen, *Senior Member, IEEE*

***Abstract*— In this article, two filtering power dividers (FPDs) with wideband and high in-band isolation, sharp bandpass selectivity, and deep out-of-band rejections based on parallel coupled lines (PCLs) and anti-parallel coupled lines (APCLs), respectively, are proposed. The open-stub loaded PCL (OSL-PCL) and open-stub loaded APCL (OSL-APCL) are, respectively, proposed, and their transmission characteristics are investigated theoretically and numerically. Based on Wilkinson power divider (WPD) topology, when a pair of OSL-PCLs are used in place of the quarter-wavelength transmission lines, the filtering characteristic is realized. The frequency selectivity is substantially enhanced by achieving transmission zeros (TZs) close to each side of the passband. To broaden the bandwidth and improve frequency selectivity and out-of-band rejection level, OSL-APCLs instead of OSL-PCLs are employed to introduce an additional TZ in the upper stopband and achieve a better out-of-band rejection. To validate these design concepts, two FPDs with center frequencies at 3.54 and 2.77 GHz are fabricated and measured, achieving good in-band isolations of more than 19 dB. The proposed OSL-APCLs-based FPD also indicates that the minimum in-band insertion loss is 3.5 dB, the 3-dB fractional bandwidth (FBW) is approximately 54.6%, and the out-of-band rejections are greater than 23 dB. The simulated and measured results are in good agreement, proving the feasibility of the proposed design strategies.**

***Index Terms*— Anti-parallel coupled line (APCL), filtering power divider (FPD), integrated design, parallel coupled line (PCL).**

Manuscript received 30 August 2023; revised 19 October 2023; accepted 23 October 2023. Date of publication 31 October 2023; date of current version 30 November 2023. This work was supported in part by the National Natural Science Foundation of China under Grant 61801059, in part by the FY2021 JSPS Postdoctoral Fellowship for Research in Japan under Grant P21053, in part by the Grant-in-Aid for JSPS Research Fellow under Grant 21F21053, in part by the Chongqing University Large Instruments and Equipment Function Development Project under Grant gnkf2023009, and in part by the Basic Research and Frontier Exploration Special of Chongqing Natural Science Foundation under Grant cstc2019jcyj-msxmX0350. Recommended for publication by Associate Editor M. Cases upon evaluation of reviewers' comments. *(Corresponding authors: Daotong Li; Ying Liu.)*

Daotong Li is with the Center of Aerocraft TT&C and Communication and the School of Microelectronics and Communication Engineering, Chongqing University, Chongqing 400044, China, and also with the Department of Communications Engineering, Tohoku University, Sendai 980-8579, Japan (e-mail: dli@cqu.edu.cn).

Luqi Zhang, Jiaxin Wang, and Ying Liu are with the School of Microelectronics and Communication Engineering, Chongqing University, Chongqing 400044, China (e-mail: liuyingcqu@cqu.edu.cn).

Qiang Chen is with the Department of Communications Engineering, Tohoku University, Sendai 980-8579, Japan.

Color versions of one or more figures in this article are available at https://doi.org/10.1109/TCPMT.2023.3328946.

Digital Object Identifier 10.1109/TCPMT.2023.3328946

I. Introduction

POWER divider performs an unrivaled crucial role in RF microwave circuits as a key component of the RF front end. Among them, the Wilkinson power divider (WPD) has been proposed and extensively employed in RF circuits. However, due to microwave devices developing toward compact, low cost, and multifunction, filtering power dividers (FPDs) have drawn increasing amounts of interest in recent years.

Bandpass filter (BPF) combined with power divider can realize power division/combination, miniaturization, and frequency selection simultaneously. Some FPDs are designed using a trigonometric substrate resonator integrated with defected ground structure [1], quarter-wavelength resonators and short-ended parallel coupled lines (PCLs) [2], several pairs of short-circuited microstrip stub resonators [3], regular triangle patch resonator [5], and ring resonators [6]. However, the abovementioned FPDs have not paid too much attention to expand their bandwidth. For the wideband application, a three-line coupled structure integrated with PCLs has been proposed to replace the T-junction of a classical WPD [7]. Although the ultrawideband response can be obtained, the isolation in the wide passband is not ideal.

A variety of FPDs have been proposed by using isolation networks, which consist of two coupled lines and lumped components [8] or a resonator, two inverters, and two resistors [9]. However, the frequency selectivity and out-of-band suppression of the designs listed above are not satisfactory enough.

In general, to design FPDs with wideband and high in-band isolation, sharp bandpass selectivity and deep out-of-band suppressions are extremely important for the RF front end. The properties of wideband, sharp bandpass selectivity, and deep out-of-band rejections in the filters are taken into account by the employment of anti-parallel coupled lines (APCLs) [12], [13]. To the best of our knowledge, papers on using APCLs to construct FPDs are very rare. Therefore, using PCL and APCL structures to construct FPDs with wideband and high in-band isolation, sharp frequency selectivity and deep out-of-band rejections are deserved to be studied.

In this article, two FPDs with wideband and high in-band isolation, sharp bandpass selectivity and deep out-of-band rejections based on PCLs and APCLs are proposed, respectively. The modified structures of open stub-loaded PCL (OSL-PCL) and open stub-loaded APCL (OSL-APCL) are,

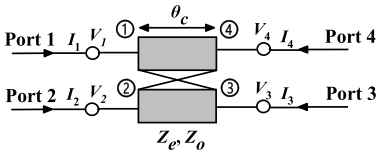

Fig. 1. Schematic of a conventional four-port PCL.

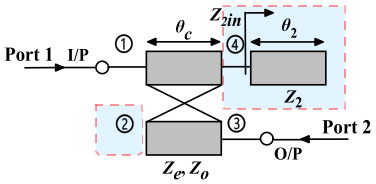

Fig. 2. Schematic of the proposed OSL-PCL.

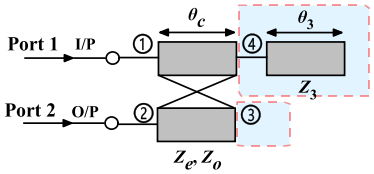

Fig. 3. Schematic of the proposed OSL-APCL.

respectively, proposed, and their transmission characteristics are analyzed theoretically. The OSL-PCLs that generate a transmission zero (TZ) on both sides of the passband and one TZ in the upper stopband are loaded to replace the 1/4 wavelength transmission lines of the classical WPD, and an FPD with high-frequency selectivity is proposed. Moreover, high isolation in the passband is achieved by loading two isolation resistors between output ports. To further improve the bandwidth, frequency selectivity, and out-of-band rejections, OSL-APCLs are used instead of the OSL-PCLs. The stopband suppressions are effectively enhanced by generating one additional TZ in the upper stopband. The results of the experiment demonstrate that the simulated and tested results are fairly consistent.

The theoretical analysis and deduction of OSL-PCL and OSL-APCL are presented in Section II. To validate the theoretical derivation, Sections III and IV provide the characteristics, simulated, and measured results of OSL-PCLs-based FPD and OSL-APCLs-based FPD, respectively. In Section V, a succinct conclusion is provided (all the designs are based on the substrate with $\varepsilon_r = 3.48$, $h = 0.508$ mm, and $\tan\delta = 0.0037$).

II. Theoretical Analysis of OSL-PCL and OSL-APCL

The schematic of a typical four-port PCL structure with its electrical length θ_c and its respective even- and odd-mode characteristic impedances Z_e and Z_o is shown in Fig. 1.

Considering that the conventional PCL is symmetrical about the central plane, the method of even- and odd-mode analysis can be used. Thus, an impedance matrix can be further derived as follows:

$$Z_{11} = Z_{22} = Z_{33} = Z_{44} = -j(Z_e + Z_o)\cot\theta_c/2 \quad (1a)$$
$$Z_{12} = Z_{21} = Z_{43} = Z_{34} = -j(Z_e - Z_o)\cot\theta_c/2 \quad (1b)$$
$$Z_{13} = Z_{31} = Z_{24} = Z_{42} = -j(Z_e - Z_o)\csc\theta_c/2 \quad (1c)$$
$$Z_{14} = Z_{41} = Z_{23} = Z_{32} = -j(Z_e + Z_o)\csc\theta_c/2. \quad (1d)$$

A. Design and Analysis of OSL-PCL

When an open stub with an electrical length of θ_2 and characteristic impedance of Z_2 is loaded at terminal ④ and terminals ① and ③ are excited, the proposed structure labeled as OSL-PCL is achieved, as shown in Fig. 2. The configuration clearly shows that the signal input from terminal ① (Port 1) of PCL and output from terminal ③ (Port 2). θ_c and θ_2 are the electrical lengths at the center frequency f_c.

The boundary conditions of terminal ② and terminal ④ are given

$$I_2 = 0 \quad (2a)$$
$$I_4 = jV_4\tan\theta_2/Z_2. \quad (2b)$$

When (2a) and (2b) is substituted, the input–output voltage relationship can be converted into a two-port Z-matrix, and by substituting (1a)–(1d), the elements of the impedance matrix of the OSL-PCL can be obtained as

$$Z_{13} = Z_{31} = -jZ_b\csc\theta_c - \frac{jZ_aZ_b\cot\theta_c\csc\theta_c\tan\theta_2}{Z_2 - Z_a\cot\theta_c\tan\theta_2} \quad (3a)$$
$$Z_{11} = -jZ_a\cot\theta_c - \frac{jZ_a^2\csc^2\theta_c\tan\theta_2}{Z_2 - Z_a\cot\theta_c\tan\theta_2} \quad (3b)$$
$$Z_{33} = -jZ_a\cot\theta_c - \frac{jZ_b^2\cot^2\theta_c\tan\theta_2}{Z_2 - Z_a\cot\theta_c\tan\theta_2} \quad (3c)$$

where

$$\begin{cases} Z_a = \dfrac{Z_e + Z_o}{2} \\ Z_b = \dfrac{Z_e - Z_o}{2}. \end{cases} \quad (4)$$

Therefore, when Ports 1 and 2 are loaded with Z_0, the transmission coefficient S_{21} of OSL-PCL can be deduced as

$$S_{21} = \frac{2Z_{31}Z_0}{(Z_{11} + Z_0)(Z_{33} + Z_0) - Z_{13}Z_{31}}. \quad (5)$$

When $S_{21} = 0$, the frequency locations of four TZs are obtained as

$$f_{TZ1} = 0 \quad (6a)$$
$$f_{TZ2} = \frac{2f_0}{\pi}\arccos\sqrt{\frac{Z_2}{(Z_o + Z_e)\tan\theta_2}} \quad (6b)$$
$$f_{TZ3} = 2f_0 - \frac{2f_0}{\pi}\arctan\left(-\frac{2Z_2}{(Z_o + Z_e)\tan\theta_2}\right) \quad (6c)$$
$$f_{TZ4} = 2f_0 \quad (6d)$$

where f_0 is the center frequency of the proposed OSL-PCL.

B. Design and Analysis of OSL-APCL

When an open stub with an electrical length of θ_3 and characteristic impedance of Z_3 is loaded at terminal ④ and terminals ① and ② are excited, the proposed structure labeled as OSL-APCL is achieved, as shown in Fig. 3. The configuration clearly shows that the signal input from terminal ① (Port 1) of APCL and output from terminal ② (Port 2).

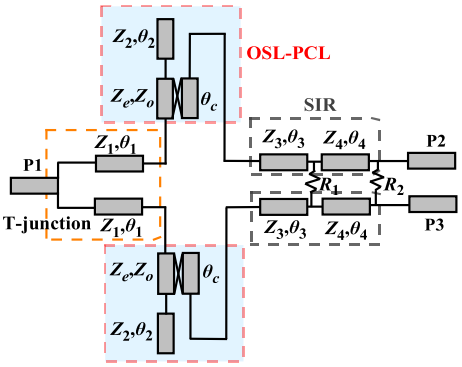

Fig. 4. Schematic of the proposed dual-mode OSL-PCLs-based FPD.

The boundary conditions of terminals ③ and ④ are given

$$I_3 = 0 \tag{7a}$$

$$I_4 = jV_4 \tan\theta_3 / Z_3 \tag{7b}$$

and the following Y matrix can be obtained:

$$Z_{12} = Z_{21} = -jZ_b \cot\theta_c - \frac{jZ_aZ_b \csc^2\theta_c \tan\theta_3}{Z_3 - Z_a \cot\theta_c \tan\theta_3} \tag{8a}$$

$$Z_{11} = -jZ_a \cot\theta_c - \frac{jZ_a^2 \csc^2\theta_c \tan\theta_3}{Z_3 - Z_a \cot\theta_c \tan\theta_3} \tag{8b}$$

$$Z_{22} = -jZ_a \cot\theta_c - \frac{jZ_b^2 \csc^2\theta_c \tan\theta_3}{Z_3 - Z_a \cot\theta_c \tan\theta_3}. \tag{8c}$$

Thus, when Ports 1 and 2 are loaded with Z_0, the S-parameter can be further derived as

$$S_{21} = \frac{-2Z_{21}Z_0}{(Z_{11}+Z_0)(Z_{22}+Z_0) - Z_{12}Z_{21}}. \tag{9}$$

Thus, the TZs can be calculated when $S_{21} = 0$ and the frequency locations of four TZs are obtained as

$$f_{TZ1} = 0 \tag{10a}$$

$$f_{TZ2} = \frac{f_0}{\pi} \arcsin\left(\frac{2(Z_e+Z_o)\tan\theta_3}{(Z_e+Z_o)\tan\theta_3 - Z_3}\right) \tag{10b}$$

$$f_{TZ3} = 2f_0 - \frac{f_0}{\pi} \arcsin\left(\frac{2(Z_e+Z_o)\tan\theta_3}{(Z_e+Z_o)\tan\theta_3 - Z_3}\right) \tag{10c}$$

$$f_{TZ4} = 2f_0. \tag{10d}$$

III. Design and Analysis of OSL-PCLs-Based FPD

Based on the classical WPD, by substituting the $\lambda/4$ transmission lines with the proposed OSL-PCLs, an FPD with the characteristics of high selectivity and high isolation is realized, as shown in Fig. 4. It consists of a T-junction, a pair of OSL-PCLs, a couple of stepped impedance lines, and two resistors R_1 and R_2. Z_1, θ_1 and Z_3, Z_4, and θ_3, θ_4 are the characteristic impedances and the electrical length of the T-junction and the stepped impedance lines, respectively.

The OSL-PCLs-based FPD can be analyzed utilizing odd-even mode analysis because of its symmetrical construction. When an even mode excites, the symmetric plane of the proposed FPD is assumed to have an ideal magnetic wall. The even-mode equivalent circuit of OSL-PCLs-based FPD is shown in Fig. 5(a); when Port 2 is well-matched, we can obtain

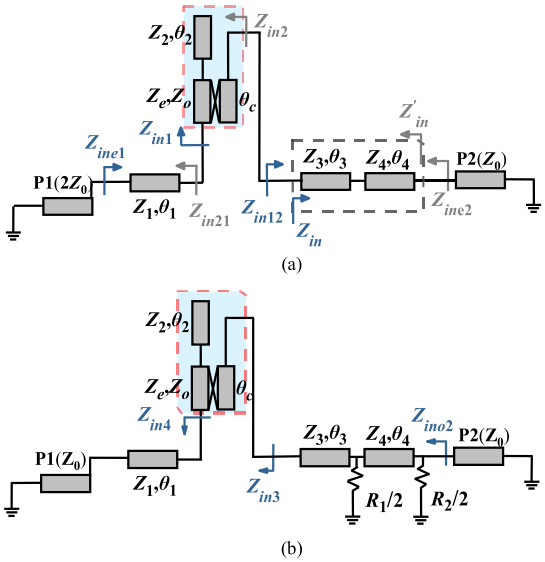

Fig. 5. Even–odd-mode analysis of the OSL-PCLs-based FPD. (a) Even-mode equivalent circuit. (b) Odd-mode equivalent circuit.

$$\Gamma_{\text{in}}^{e} = \frac{Z_{\text{in}e1} - 2Z_0}{Z_{\text{in}e1} + 2Z_0} \tag{11}$$

where

$$Z_{\text{in}e1} = Z_1 \frac{Z_{\text{in}1} + jZ_1 \tan\theta_1}{Z_1 + jZ_{\text{in}1} \tan\theta_1} \tag{12a}$$

$$Z_{\text{in}1} = Z_{11} - \frac{Z_{13}Z_{31}}{Z_{\text{in}2} + Z_{33}} \tag{12b}$$

$$Z_{\text{in}2} = Z'_{\text{in}} \frac{Z_0 + jZ'_{\text{in}}}{Z'_{\text{in}} + jZ_0} \tag{12c}$$

$$Z'_{\text{in}} = Z_4 \frac{-jZ_3 \tan\theta_3 + jZ_4 \tan\theta_4}{Z_4 + Z_3 \tan\theta_3 \tan\theta_4}. \tag{12d}$$

When Port 1 is well-matched, the reflection coefficient can be obtained from (15)

$$\Gamma_{\text{out}}^{e} = \frac{Z_{\text{in}e2} - Z_0}{Z_{\text{in}e2} + Z_0} \tag{13}$$

where

$$Z_{\text{in}e2} = Z_{\text{in}2} \frac{Z_{\text{in}2} + jZ_{\text{in}}}{Z_{\text{in}} + jZ_{\text{in}2}} \tag{14a}$$

$$Z_{\text{in}2} = Z_{11} - \frac{Z_{13}Z_{31}}{Z_{\text{in}21} + Z_{11}} \tag{14b}$$

$$Z_{\text{in}21} = Z_1 \frac{2Z_0 + jZ_1 \tan\theta_1}{Z_1 + j2Z_0 \tan\theta_1} \tag{14c}$$

$$Z_{\text{in}} = Z_3 \frac{-jZ_4 \tan\theta_4 + jZ_3 \tan\theta_3}{Z_3 + Z_4 \tan\theta_3 \tan\theta_4}. \tag{14d}$$

When an odd mode excites, the symmetric plane of the proposed FPD is assumed to have an ideal conductive wall. The odd-mode equivalent circuit of OSL-PCLs-based FPD is shown in Fig. 5(b). When Port 1 is perfectly matched, Γ_{out}^{o} can be obtained through (18)

$$\Gamma_{\text{out}}^{o} = \frac{Z_{\text{in}o2} - Z_0}{Z_{\text{in}o2} + Z_0} \tag{15}$$

where

$$Z_{ino2} = \frac{R_2 \times Z_{in3}}{R_2 + 2Z_{in3}} \tag{16a}$$

$$Z_{in3} = Z_4 \frac{Z_{in4} + jZ_4 \tan\theta_4}{Z_4 + jZ_{in4} \tan\theta_4} \tag{16b}$$

$$Z_{in4} = \frac{R_1 \times Z_{in5}}{R_1 + 2Z_{in5}} \tag{16c}$$

$$Z_{in5} = Z_3 \frac{Z_{in6} + jZ_3 \tan\theta_3}{Z_3 + jZ_{in6} \tan\theta_3} \tag{16d}$$

$$Z_{in6} = Z_{11} - \frac{Z_{13}Z_{31}}{Z_{in7} + Z_{11}} \tag{16e}$$

$$Z_{in7} = Z_1 \frac{Z_0 + jZ_1 \tan\theta_1}{Z_1 + jZ_0 \tan\theta_1}. \tag{16f}$$

Therefore, the S-parameters can be expressed as

$$S_{11} = \frac{\Gamma^e_{in} + \Gamma^e_{out}}{2} \tag{17a}$$

$$S_{12} = S_{21} = \frac{\Gamma^e_{in} - \Gamma^e_{out}}{2} \tag{17b}$$

$$S_{22} = S_{33} = \frac{\Gamma^e_{out} + \Gamma^o_{out}}{2} \tag{17c}$$

$$S_{32} = \frac{\Gamma^e_{out} - \Gamma^o_{out}}{2}. \tag{17d}$$

Based on the theoretical analysis of Sections II and III, the design processes of the proposed OSL-PCL-based FPD can be written as follows.

1) First, according to the desired design specifications, the required design parameters, such as center frequency (f_0), 3-dB FBW, and frequency selectivity, of the designed FPD can be determined.
2) Assuming that the electrical length of PCL $\theta_c = 90°$, the locations of the TZs are determined by the required frequency selectivity. The electrical length of the open stub $\theta_2 = 180°$ of the corresponding frequencies can be deduced according to (6).
3) According to the desired design bandwidth determined in step (1), the odd- and even-mode impedance $Z_e = 200\ \Omega$, $Z_o = 73\ \Omega$, and $Z_c = 121\ \Omega$, coupling coefficient $k = 0.46$, and the impedance of other transmission lines $Z_1 = 60\ \Omega$, $Z_2 = 44\ \Omega$, $Z_3 = 40\ \Omega$, and $Z_4 = 79\ \Omega$ with its corresponding electrical length $\theta_1 = 20°$, $\theta_3 = 70°$, and $\theta_4 = 70°$ can be calculated according to (11)–(17).
4) Finally, the isolation resistance is determined as $R_1 = R_2 = (2Z_{ine2}Z_3/(Z_{in3} - Z_{ine2})) = 100\ \Omega$ according to (17d), and the obtained circuit parameters are converted into actual physical dimensions, and then further, a fine optimization is carried out.

Based on the analysis above, an OSL-PCLs-based FPD is constructed, as shown in Fig. 6, and the PCLs and open stubs are folded to reduce the overall size of the FPD.

To further gain insight into the working mechanism of the proposed OSL-PCLs-based FPD, the impacts of some key parameters on the performance are analyzed numerically.

Fig. 7(a) illustrates the change of coupling coefficient k and 3-dB fractional bandwidth (FBW) with different W_1 and S values. When $W_1 = 0.1$ mm is fixed, with the gap S of the PCL increasing from 0.1 to 0.3 mm, k decreases from

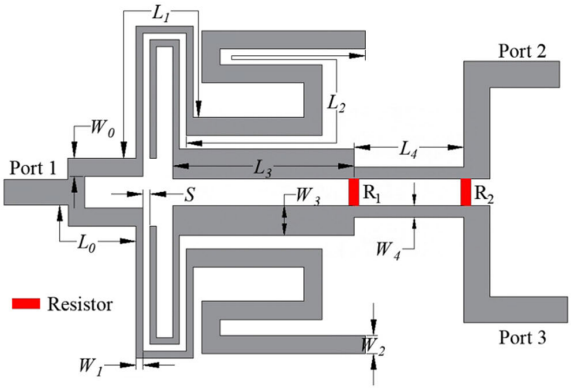

Fig. 6. Layout of the proposed dual-mode OSL-PCLs-based FPD.

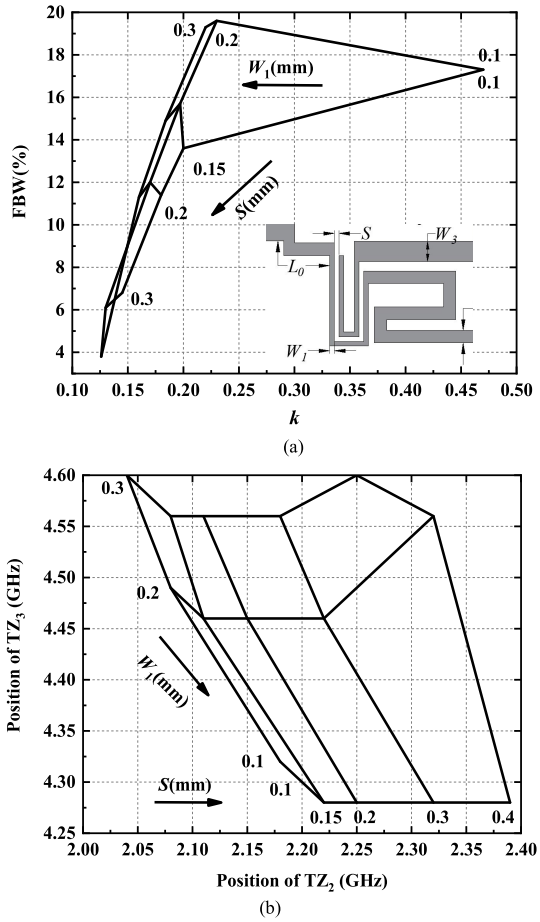

Fig. 7. (a) Coupling coefficient k and 3-dB FBW versus with different W_1 and S values. (b) Position of TZ_2 and TZ_3 versus with different W_1 and S values.

0.46 to 0.22, and the FBW becomes narrower from 17.3% to 3.4%. Compared with W_1, S has less influence on k and FBW. When W_1 and S increase, it can be seen that k and FBW decrease significantly. Fig. 7(b) exhibits the position change of TZ_2 and TZ_3 with different W_1 and S values. When $S = 0.1$ mm is fixed, with the width W_1 of the PCL decreasing from 0.3 to 0.1 mm, TZ_2 moves from 2 to 2.2 GHz, and TZ_3 moves from 4.6 to 4.3 GHz, and since both the TZ_2 and TZ_3 move toward the center frequency, the frequency selectivity of the passband becomes better. When W_1 is fixed, TZ_2 moves toward high frequency with the increase of S, while TZ_3 has

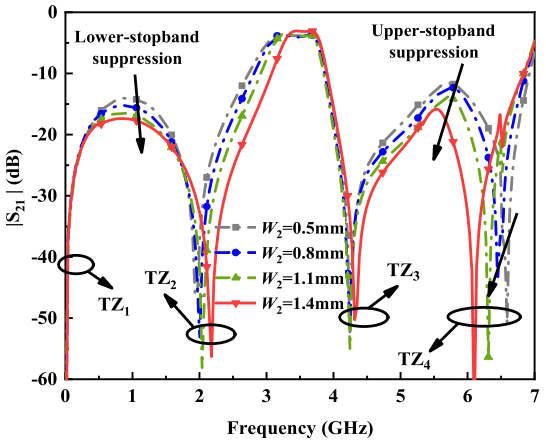

(a)

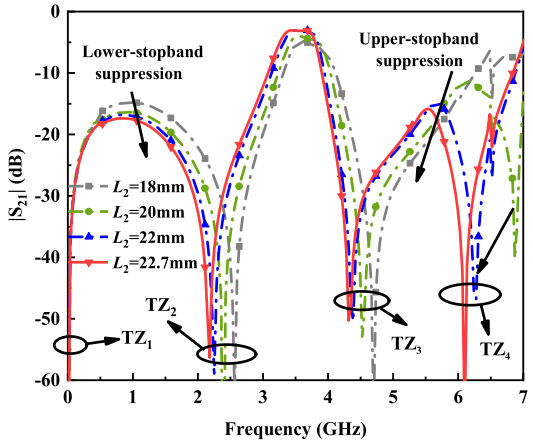

(b)

Fig. 8. Simulated S_{21} versus (a) W_2 and (b) L_2, respectively.

less influence. Thus, the coupling coefficient k, FBW, and frequency selectivity can be adjusted by changing W_1 and S.

Fig. 8(a) exhibits the simulated transmission coefficient with $W_2 = 0.5$, 0.8, 1.1, and 1.4 mm, under the condition of $L_2 = 22.7$ mm. Fig. 8(b) exhibits the simulated transmission coefficient with $L_2 = 18$, 20, 22, and 22.7 mm, under the condition of $W_2 = 1.4$ mm. As W_2 increases from 0.5 to 1.4 mm, the lower stopband suppression is changed from 14 to 17 dB, and the upper stopband suppression is enhanced from 12 to 16 dB. As L_2 increases from 18 to 22.7 mm, the lower and upper stopband suppressions are improved from 15 and 7 to 17 and 16 dB, respectively. In a conclusion, the width and length of open stubs can be changed to control the out-of-band suppressions, which satisfies the theoretical analysis in Section II.

To demonstrate the effectiveness of the above design concept, a demonstration of OSL-PCLs-based FPD is designed, fabricated, and tested on Rogers 4350B substrate. The dielectric substrate has a thickness of $h = 0.508$ mm, a dielectric constant of $\varepsilon_r = 3.48$, and a loss tangent of $\tan\delta = 0.0037$. The isolation resistors R_1 and R_2 are 0603 packaged chip resistors. Fig. 9 shows the photograph of fabricated FPD based on OSL-PCLs, and the determined fabricated and calculated structure parameters are shown in Table I. The effective circuit area of OSL-PCLs-based FPD is $0.39\lambda_g \times 0.55\lambda_g$, where λ_g is the waveguide wavelength at the center frequency.

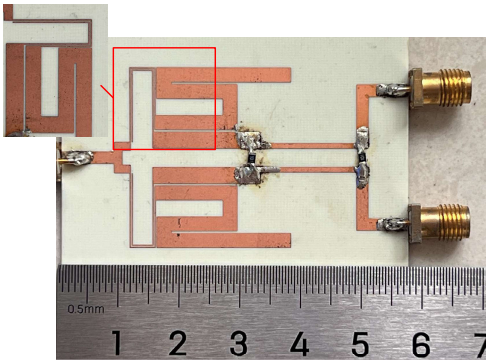

Fig. 9. Photograph of OSL-PCLs-based FPD.

TABLE I

PARAMETERS OF OSL-PCL-BASED FPD AND OSL-APCL-BASED FPD (SUBSTRATE: $\varepsilon_r = 3.48$, $h = 0.508$ mm, AND $\tan\delta = 0.0037$)

Designed FPDs	Circuit parameters	Layout parameters
OSL-PCL-based FPD	Z_e=200Ω, Z_o=73Ω, Z_c=121Ω, Z_1=60Ω, Z_2=44Ω, Z_3=40Ω, Z_4=79Ω, R_1=R_2=100Ω,θ_1=20°, θ_2=180°, θ_3=70°, θ_4=70°, R_1=100Ω, R_2=100Ω	W_0=0.8mm, W_1=0.1mm, W_2=1.4mm, W_3=1.6mm, W_4=0.6mm, S=0.1mm, L_0=2.4mm, L_1=15mm, L_2= 22.7mm, L_3=10.4mm, L_4=10.5mm
OSL-APCL-based FPD	Z_e=200Ω, Z_o=73Ω, Z_c=121Ω, Z_1=140Ω, Z_2=62Ω, Z_3=17Ω, Z_4=40Ω,θ_c=90°,θ_1=40°, θ_2=120°, θ_3=180°, θ_4=65°, R_1=10Ω, R_2=100Ω	W_0=0.1mm, W_1=0.1mm, W_2=1mm, W_3=4.8mm, W_4=1.6mm, S=0.1mm, L_0= 8.3mm, L_1=16.6mm, L_2 =20mm, L_3 =30.5mm, L_4=12.6mm

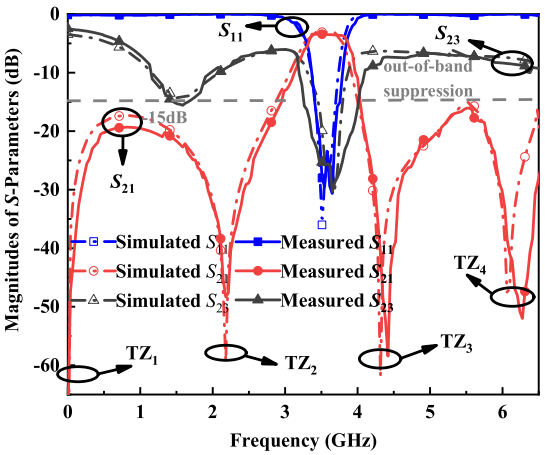

Fig. 10. Comparison of tested and simulated results of S-parameters on OSL-PCLs-based FPD.

The simulated and measured results of the proposed OSL-PCL-based FPD are shown in Fig. 10. According to the measured results, the proposed OSL-PCLs-based FPD centers at 3.54 GHz with a 17.3% 3-dB FBW ranging from 3.23 to 3.84 GHz. The measured in-band insertion loss is 3.4 dB, return loss is greater than 20 dB, and in-band isolation is higher than 25 dB. Besides, the out-of-band rejections are better than 15 dB. Four TZs generated by OSL-PCLs, located at 0, 2.2, 4.3, and 6.1 GHz, resulting in high-frequency selectivity and deep out-of-band rejections. The tested results are compatible with the simulated results, as shown by a comparison between the simulated and measured data. Fig. 11

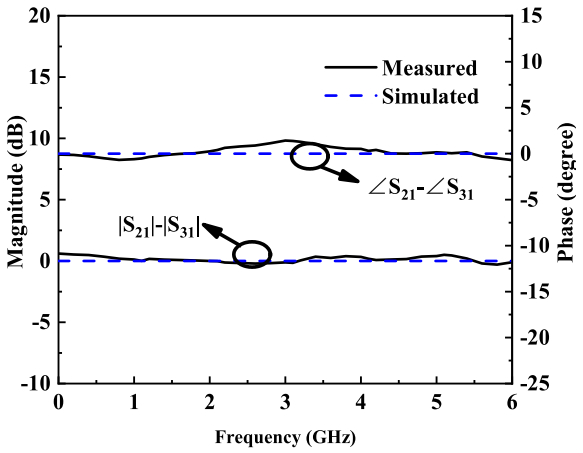

Fig. 11. Simulated and measured magnitude and phase difference between two output ports of OSL-PCL-based FPD.

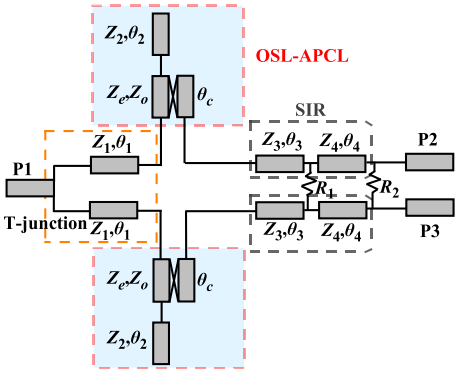

Fig. 12. Schematic of the proposed dual-mode OSL-APCLs-based FPD.

shows the magnitude and phase differences between the two output ports, where the in-band amplitude imbalance is less than ± 0.7 dB, and the phase difference within the passband is less than $\pm 1.6°$.

IV. Design and Analysis of OSL-APCLs-Based FPD

According to the analysis in Section II, the OSL-APCL can further improve the bandwidth and out-of-band suppression level. By replacing the OSL-PCLs in Section III with OSL-APCLs, the proposed OSL-APCLs-based FPD with enhanced bandwidth and out-of-band performance can be achieved. The circuit structure of the OSL-APCLs-based FPD is shown in Fig. 12. It can be found that the circuit structure is symmetrical, and the analysis method of even and odd modes can also be used to derive the design formula for this FPD. By using the same analysis method as Section III and substituting (17a)–(17d), the S-parameters of OSL-APCL-based FPD can be calculated as well.

As shown in Fig. 13, an OSL-APCLs-based FPD is constructed by the same design processes of OSL-PCLs-based FPD in Section III. Similarly, the APCLs and the open stubs are folded to reduce the overall size.

To learn more about the working mechanism of the proposed FPD based on OSL-APCLs, the impacts of some key parameters on the performance are analyzed numerically, as shown in Fig. 14. From Fig. 14, we can see obviously that the 3-dB FBW of OSL-APCLs-based FPD is about 54.6%,

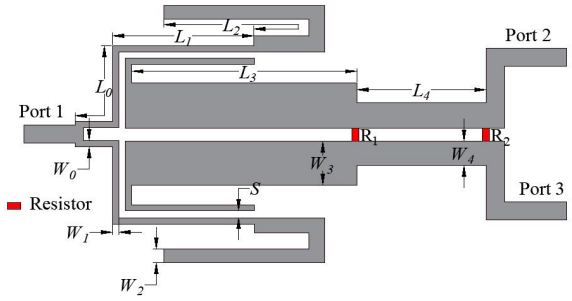

Fig. 13. Layout of the proposed dual-mode OSL-APCLs-based FPD.

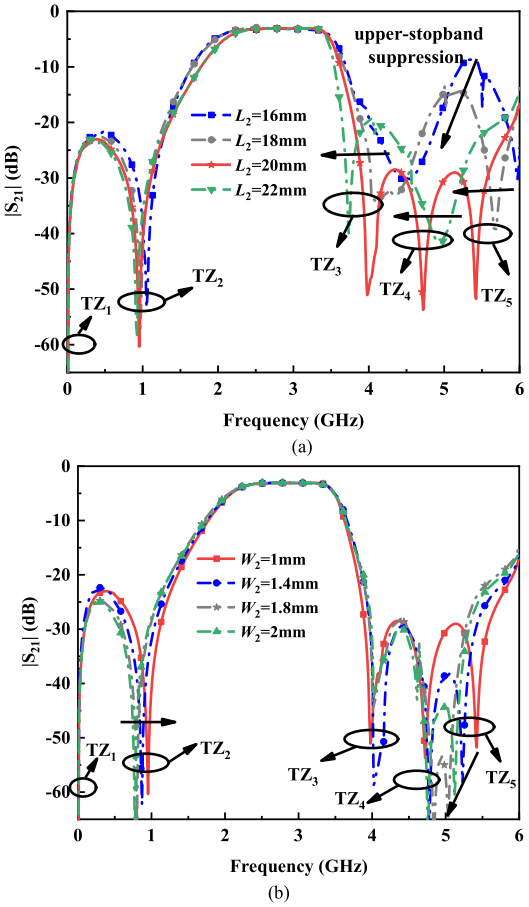

Fig. 14. Simulated S_{21} versus (a) L_2 and (b) W_2, respectively.

which is much wider than that of OSL-PCLs-based FPD in Section III. As shown in Fig. 14, there are TZs TZ_2 and TZ_3 on both sides of the passband. Compared to the OSL-PCL structure, TZ_5 is the second harmonic TZ of the OSL-APCL, which is close to TZ_3 and TZ_4. The three TZs TZ_3, TZ_4, and TZ_5 in the upper stopband effectively improve the out-of-band rejection. Fig. 14(a) shows the transmission coefficient of OSL-APCL-based FPD with $L_2 = 16$, 18, 20, and 22 mm, under the condition of $W_2 = 1$ mm. It can be seen that when L_2 increases, TZ_3, TZ_4, and TZ_5 move toward center frequency, and the upper stopband suppression becomes deeper. Moreover, when L_2 increases, TZ_4 and TZ_5 get closer. Fig. 14(b) shows the transmission coefficient of the proposed FPD with the width W_2 versus from 1 to 2 mm, under the condition of $L_2 = 20$ mm. When W_2 decreases, TZ_2 moves from 0.76 to 1 GHz with the constant absolute bandwidth,

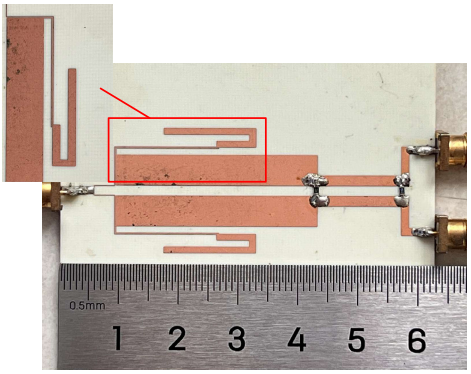

Fig. 15. Photograph of OSL-APCLs-based FPD.

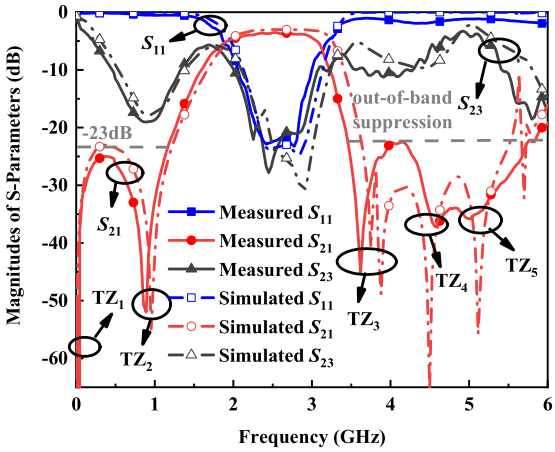

Fig. 16. Comparison of tested and simulated results of S-parameters on OSL-PCLs-based FPD.

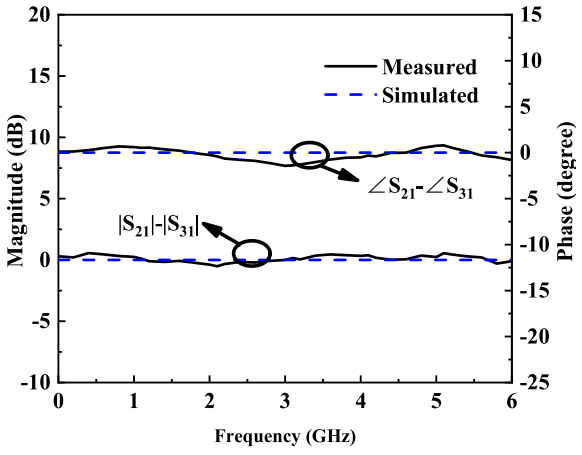

Fig. 17. Simulated and measured magnitude and phase difference between two output ports of OSL-APCL-based FPD.

and the frequency selectivity becomes better. Thus, the out-of-band rejections and frequency selectivity are impacted by the length L_2 and width W_2 of open stubs loaded on the APCLs.

Fig. 15 displays the photograph of fabricated OSL-APCLs-based FPD, and its fabricated and calculated structure parameters are shown in Table I. The circuit area is $0.34\lambda_g \times 0.82\lambda_g$. The comparison of the measured and simulated S-parameters for the OSL-APCLs-based FPD is shown in Fig. 16. The measured in-band insertion loss is 3.5 dB, the return loss is better than 20 dB, and the in-band isolation is higher than 19 dB in the working frequency band of 2.49–3.29 GHz. The 3-dB FBW is around 54.6% ranging from 2.01 to 3.52 GHz. The measured results show the five TZs located in 0, 0.95, 3.98, 4.66, and 5.12 GHz, respectively, resulting in out-of-band rejections better than 23 dB. Fig. 17 shows the magnitude and phase differences between the two output ports, where the in-band amplitude imbalance is less than ±0.6 dB, and the phase difference within the passband is less than ±1.5°.

TABLE II
COMPARISON WITH OTHER PREVIOUS WORKS

Refs.	f_0(GHz)/ FBW(%)	IL (dB)	RL (dB)	Iso. (dB)	Rej. (dB)	SF	Size($\lambda_g \times \lambda_g$)
[3]	2/5	5.1	10	43	N.A	2.9	0.9×3.79
[5]	1.27/7	4.2	15	20	25	4.4	0.68×0.6
[6]	3.5/9.2	4	20	10	20	3.1	1×0.8
[9]	1/15	4.3	30	18	20	3.6	0.81×0.6
[14]	4/13.7	4.38	19.5	23	20	4	0.88×0.97
Work I	**3.54/17.3**	**3.4**	**20**	**25**	**15**	**2.6**	**0.39×0.55**
Work II	**2.77/54.6**	**3.5**	**20**	**19**	**23**	**1.7**	**0.34×0.82**

Refs.: References; FBW: 3-dB fractional bandwidth; IL: Insertion Loss; RL: ReturnLoss; Iso.: In-band isolation; Rej.: Out-of-band rejection; SF: Shape factor SF = $(f_2^{25dB}\text{-}f_1^{25dB})$ / $(f_2^{3dB}\text{-}f_1^{3dB})$

To highlight the advantages of this article, Table II provides a summary of the contrast between the proposed FPDs in this work and the recently reported counterparts. It can be concluded that our design shows the merits of wide operation passband and high in-band isolation, sharp frequency selectivity, and high out-of-band rejections, simultaneously.

V. CONCLUSION

In this article, two FPDs based on OSL-PCLs and OSL-APCLs with wideband and high in-band isolation, sharp bandpass selectivity, and deep out-of-band rejections are presented, respectively. The structures of OSL-PCL and OSL-APCL are proposed and their transmission characteristics are investigated theoretically and numerically. Then, the OSL-PCLs are adopted in the Wilkinson topology to obtain a high-selectivity FPD. By replacing OSL-PCLs with OSL-APCL, an FPD with wider bandwidth, sharper bandpass selectivity, and deeper out-of-band rejection is further constructed. To verify the effectiveness of the design ideas, FPDs with center frequencies at 3.54 and 2.77 GHz are fabricated and tested, respectively. The measured results of the OSL-APCLs-based FPD show that the 3-dB FBW is 54.6%, and the in-band isolation and out-of-band rejection are better than 19 and 23 dB, respectively. In comparison to other designs, the suggested structure has a wide operation passband, sharp bandpass selectivity, and deep out-of-band suppression level. It is a good candidate for the compact microwave-integrated circuit design.

REFERENCES

[1] Q. Li, H. Tang, D. Tang, Z. Deng, and X. Luo, "Compact SIDGS filtering power divider with three-port 10-GHz reflectionless range," *IEEE Trans. Circuits Syst. II, Exp. Briefs*, vol. 69, no. 7, pp. 3129–3133, Jul. 2022.

[2] M. Fan, K. Song, L. Yang, and R. Gómez-Garcia, "Frequency-reconfigurable input-reflectionless bandpass filter and filtering power divider with constant absolute bandwidth," *IEEE Trans. Circuits Syst. II, Exp. Briefs*, vol. 68, no. 7, pp. 2424–2428, Jul. 2021.

[3] B. Lee, J. Lee, G. Lee, and J. Lee, "All-port-reflectionless narrowband filtering power divider topology with generic equations," *IEEE Trans. Circuits Syst. I, Reg. Papers*, vol. 69, no. 4, pp. 1417–1426, Apr. 2022.
[4] G. Shen, W. Che, W. Feng, and Q. Xue, "High-isolation topology for filtering power dividers based on complex isolation impedance and surface wave suppression," *IEEE Trans. Microw. Theory Techn.*, vol. 69, no. 1, pp. 43–53, Jan. 2021.
[5] Y. Zhu, J. Wang, J. Hong, J.-X. Chen, and W. Wu, "Two- and three-way filtering power dividers with harmonic suppression using triangle patch resonator," *IEEE Trans. Circuits Syst. I, Reg. Papers*, vol. 68, no. 12, pp. 5007–5017, Dec. 2021.
[6] W. Feng, W. Che, Y. Shi, Q. Xue, Y. C. Li, and X. Y. Zhou, "High selectivity balanced-to-unbalanced filtering power dividers using dual-mode ring resonators," *IEEE Trans. Compon., Packag., Manuf. Technol.*, vol. 9, no. 5, pp. 927–935, May 2019.
[7] X. Yu and S. Sun, "A novel wideband filtering power divider with embedding three-line coupled structures," *IEEE Access*, vol. 6, pp. 41280–41290, 2018.
[8] C.-J. Chen, "A coupled-line isolation network for the design of filtering power dividers with improved isolation," *IEEE Trans. Compon., Packag., Manuf. Technol.*, vol. 8, no. 10, pp. 1830–1837, Oct. 2018.
[9] B. Lee, S. Nam, and J. Lee, "Filtering power divider with reflectionless response and wide isolation at output ports," *IEEE Trans. Microw. Theory Techn.*, vol. 67, no. 7, pp. 2684–2692, Jul. 2019.
[10] K. Xu, Y. Bai, C. Zhu, and Y. Liu, "Design of filtering power divider with high frequency selectivity," *Microw. Opt. Technol. Lett.*, vol. 60, no. 7, pp. 1649–1653, May 2018.
[11] Y. Liu, S. Sun, and L. Zhu, "2n-way wideband filtering power dividers with good isolation enhanced by a modified isolation network," *IEEE Trans. Microw. Theory Techn.*, vol. 70, no. 6, pp. 3177–3187, Jun. 2022.
[12] C. P. Chiang and K. W. Tam, "Compact quasi-elliptic microstrip bandpass filter using terminated anti-parallel coupled-line," *IET Microw., Antennas Propag.*, vol. 3, pp. 1206–1210, Jan. 2010.
[13] L. Wang and L. Jin, "A quasi-elliptic microstrip bandpass filter using modified anti-parallel coupled-line," *Prog. Electromagn. Res.*, vol. 138, pp. 245–253, 2013.
[14] F. Huang and L. Zhu, "Balanced-to-unbalanced filtering in-phase power divider based on 2-D patch resonator," *IEEE Microw. Wireless Technol. Lett.*, vol. 33, no. 4, pp. 399–402, Apr. 2023.
[15] Y.-H. Zhu, J. Cai, Y. Cao, and J.-X. Chen, "Compact wideband absorptive filtering power divider with a reused composite T-shape network," *IEEE Trans. Circuits Syst. II, Exp. Briefs*, vol. 70, no. 3, pp. 899–903, Mar. 2023.
[16] D. Wang, X. Guo, and W. Wu, "Wideband unequal power divider with enhanced power dividing ratio, fully matching bandwidth, and filtering performance," *IEEE Trans. Microw. Theory Techn.*, vol. 70, no. 6, pp. 3200–3212, Jun. 2022.
[17] J.-K. Xiao, X.-Y. Yang, and X.-F. Li, "A 3.9 GHz/63.6% FBW multimode filtering power divider using self-packaged SISL," *IEEE Trans. Circuits Syst. II, Exp. Briefs*, vol. 68, no. 6, pp. 1842–1846, Jun. 2021.
[18] Y. Liu, S. Sun, and L. Zhu, "Design of n-way wideband filtering power dividers with good port–port isolation," *IEEE Trans. Microw. Theory Techn.*, vol. 69, no. 7, pp. 3298–3306, Jul. 2021.
[19] J.-X. Xu, M. Huang, W.-L. Zhan, and X. Y. Zhang, "Reconfigurable filtering power divider with arbitrary operating channels based on external quality factor control," *IEEE Trans. Circuits Syst. I, Reg. Papers*, vol. 69, no. 11, pp. 4395–4403, Nov. 2022.
[20] Y.-S. Lin and K.-S. Lan, "Realization of a compact and high-performance power divider using parallel RC isolation network," *IEEE Trans. Circuits Syst. II, Exp. Briefs*, vol. 68, no. 4, pp. 1368–1372, Apr. 2021.

Daotong Li (Senior Member, IEEE) received the Ph.D. degree in electromagnetic field and microwave technology from the University of Electronic Science and Technology of China (UESTC), Chengdu, China, in 2016.

In 2017, he joined the Center of Communication and Tracking Telemetry Command, Chongqing University, Chongqing, China, as an Assistant Professor, where he was promoted to Associate Professor in 2019. Since 2015, he has been a Visiting Researcher with the Department of Electrical and Computer Engineering, University of Illinois at Urbana–Champaign, Urbana, IL, USA, with financial support from the China Scholarship Council. Since November 2021, he has been the Japan Society for the Promotion of Science (JSPS) Fellow with the Department of Communications Engineering, Graduate School of Engineering, Tohoku University, Sendai, Japan. He is currently with the Center of Communication and Tracking Telemetry Command, Chongqing University. He has authored or coauthored more than 100 peer-reviewed journal and conference papers. His current research interests include RF, microwave and millimeter-wave technology and applications, microwave power transmission (MPT), antennas, devices, circuits and systems, and passive and active (sub-)millimeter-wave imaging and radiometer.

Dr. Li was a recipient of the UESTC Outstanding Graduate Award by the Sichuan province and UESTC in 2016; the National Graduate Student Scholarship from the Ministry of Education, China; and the "Tang Lixin" Scholarship. He received the Fellowship from JSPS. He serves as a reviewer for several IEEE and IET journals and many international conferences as a TPC Member, a Session Organizer, and the Session Chair.

Luqi Zhang received the B.E. degree in electronic information science and technology from China West Normal University, Nanchong, China, in 2021. She is currently pursuing the M.S degree in information and communication engineering with Chongqing University, Chongqing, China.

Her current research interests include planar multifunctional microwave and millimeter-wave passive components.

Jiaxin Wang (Graduate Student Member, IEEE) received the B.E. degree in electromagnetic fields and wireless technology from the Chongqing University of Posts and Telecommunications, Chongqing, China, in 2021. She is currently pursuing the M.S. degree in electronic and information engineering with Chongqing University, Chongqing.

Her current research interests include mm-wave planar self-packaged filtering circuits.

Ying Liu received the B.E. degree in communications engineering from the Qingdao University of Science and Technology, Qingdao, Shandong, China, in 2012, and the M.S. degree in communication and information system from Chongqing University, Chongqing, China, in 2015.

She is currently with the School of Microelectronics and Communication Engineering, Chongqing University. Her current research interests include microwave and optical image processing and microwave photonics.

Qiang Chen (Senior Member, IEEE) received the B.E. degree from Xidian University, Xi'an, China, in 1986, and the M.E. and D.E. degrees from Tohoku University, Sendai, Japan, in 1991 and 1994, respectively.

He is currently the Chair Professor of the Electromagnetic Engineering Laboratory, Department of Communications Engineering, Faculty of Engineering, Tohoku University. His primary research interests include antennas, microwave and millimeter wave, electromagnetic measurement, and computational electromagnetics.

Dr. Chen received the Best Paper Award and the Zen-ichi Kiyasu Award from the Institute of Electronics, Information and Communication Engineers (IEICE). He served as the Chair for IEICE Technical Committee on Photonics-applied Electromagnetic Measurement from 2012 to 2014, IEICE Technical Committee on Wireless Power Transfer from 2016 to 2018, IEEE Antennas and Propagation Society Tokyo Chapter from 2017 to 2018, and IEICE Technical Committee on Antennas and Propagation from 2019 to 2021. He is a Fellow of IEICE.